Check for updates

A singlet-triplet hole spin qubit in planar Ge

Daniel Jirovec [1✉], Andrea Hofmann[1], Andrea Ballabio[2], Philipp M. Mutter [3], Giulio Tavani[2], Marc Botifoll[4], Alessandro Crippa[1], Josip Kukucka[1], Oliver Sagi[1], Frederico Martins [1], Jaime Saez-Mollejo[1], Ivan Prieto[1], Maksim Borovkov[1], Jordi Arbiol [4,5], Daniel Chrastina [2], Giovanni Isella [2] and Georgios Katsaros [1✉]

Spin qubits are considered to be among the most promising candidates for building a quantum processor. Group IV hole spin qubits are particularly interesting owing to their ease of operation and compatibility with Si technology. In addition, Ge offers the option for monolithic superconductor–semiconductor integration. Here, we demonstrate a hole spin qubit operating at fields below 10 mT, the critical field of Al, by exploiting the large out-of-plane hole *g*-factors in planar Ge and by encoding the qubit into the singlet-triplet states of a double quantum dot. We observe electrically controlled *g*-factor difference-driven and exchange-driven rotations with tunable frequencies exceeding 100 MHz and dephasing times of 1 μs, which we extend beyond 150 μs using echo techniques. These results demonstrate that Ge hole singlet-triplet qubits are competing with state-of-the-art GaAs and Si singlet-triplet qubits. In addition, their rotation frequencies and coherence are comparable with those of Ge single spin qubits, but singlet-triplet qubits can be operated at much lower fields, emphasizing their potential for on-chip integration with superconducting technologies.

H oles in Ge have emerged as one of the most promising spin qubit candidates[1] because of their particularly strong spin–orbit coupling[2], which leads to record manipulation speeds[3] and low dephasing rates[4]. In addition, the spin–orbit coupling, together with the low effective mass[5], relaxes fabrication constraints, and larger quantum dots can be operated as qubits without the need for microstrips and micromagnets. In only three years, single Loss–DiVincenzo qubit[6], two-qubit and most recently even four-qubit devices have been demonstrated[7–9]. Here we show that by implementing Ge hole spin qubits in a double quantum dot device, they have the further appealing feature that operation below the critical field of aluminium becomes possible.

In order to realize such a qubit, a strained Ge quantum well (QW) structure with a hole mobility of $1.0 \times 10^5 \, \text{cm}^2 \, \text{V}^{-1} \, \text{s}^{-1}$ at a density of $9.7 \times 10^{11} \, \text{cm}^{-2}$ was grown by low-energy plasma-enhanced chemical vapour deposition. Starting from a Si wafer, a 10-μm-thick strain-relaxed $Si_{0.3}Ge_{0.7}$ virtual substrate (VS) is obtained by linearly increasing the Ge content during the epitaxial growth. The ~20-nm-thick strained Ge QW is then deposited and capped by 20 nm of $Si_{0.3}Ge_{0.7}$. In Fig. 1a we show the aberration-corrected high-angle annular dark-field (HAADF) scanning transmission electron microscopy image of our heterostructure. The HAADF Z contrast clearly draws the sharp interfaces between the QW and the top and bottom barriers. In addition, X-ray diffraction measurements highlight the lattice matching between the virtual substrate and the QW (Fig. 1b). Holes confined in such a QW are of mainly the heavy-hole (HH) type because compressive strain and confinement move light-holes (LHs) to higher hole energies[10]. The related Kramers doublet of the spin $S_Z = \pm 3/2$ states therefore resembles an effective spin-1/2 system, $|\uparrow\rangle$ and $|\downarrow\rangle$.

In a singlet-triplet qubit, the logical quantum states are defined in a two-spin-1/2 system with total spin along the quantization axis $S_Z = 0$ (refs. [11,12]). This is achieved by confining one spin in each of two tunnel coupled quantum dots, formed by depletion gates (Fig. 1c). We tune our device into the single hole transport regime, as shown by the stability diagram in Fig. 2a where the sensor dot reflected phase signal (Φ_{refl}) is displayed as a function of the voltage on gates L and R (Methods and Supplementary Figs. 7 and 8). Each Coulomb blocked region corresponds to a fixed hole occupancy, and is labelled by (N_L, N_R), with N_L (N_R) being the equivalent number of holes in the left (right) quantum dot; interdot and dot to-lead charge transitions appear as steep changes in the sensor signal. Fast pulses are applied to the outer barrier gates LB and RB, which eases pulse calibration since the cross capacitance to the opposite dot is negligible. By pulsing in a clockwise manner along the empty–separate–measure (E–S–M) vertices (Fig. 2b), we observe a triangular region leaking inside the upper-left Coulomb blocked region. Such a feature identifies the metastable region where the Pauli spin blockade occurs: once initialized in E, the pulse to S loads a charge, and the spins are separated, forming either a spin singlet or a triplet. At the measurement point M within the marked triangle, the spin singlet state leads to tunnel events, while the triplet states remain blocked, which allows spin-to-charge conversion. We repeat the experiment with a counter-clockwise ordering (E–M–S) and no metastable region is observed, as expected (Fig. 2a was acquired while pulsing in the counter-clockwise ordering).

We thus consider the interdot line across the detuning (ϵ) axis of Fig. 2a equivalent to the $(2,0) \leftrightarrow (1,1)$ effective charge transitions. The system is tuned along the detuning axis from (2,0) to (1,1) by applying opposite pulses at radio frequency (rf) of amplitude V_{rf} on LB and RB: $\epsilon = V_{\text{rf}} \sqrt{\alpha_{\text{rfLB}}^2 + \alpha_{\text{rfRB}}^2}$ (Supplementary Fig. 7), where α_{rfLB} (α_{rfRB}) is the rf-lever arm of the left (right) barrier gate. The double quantum dot spectrum for a finite magnetic field B is reported in Fig. 2c (the triplet states $T(2,0)$ lie high up in energy and are not shown; the model Hamiltonian is derived in Supplementary
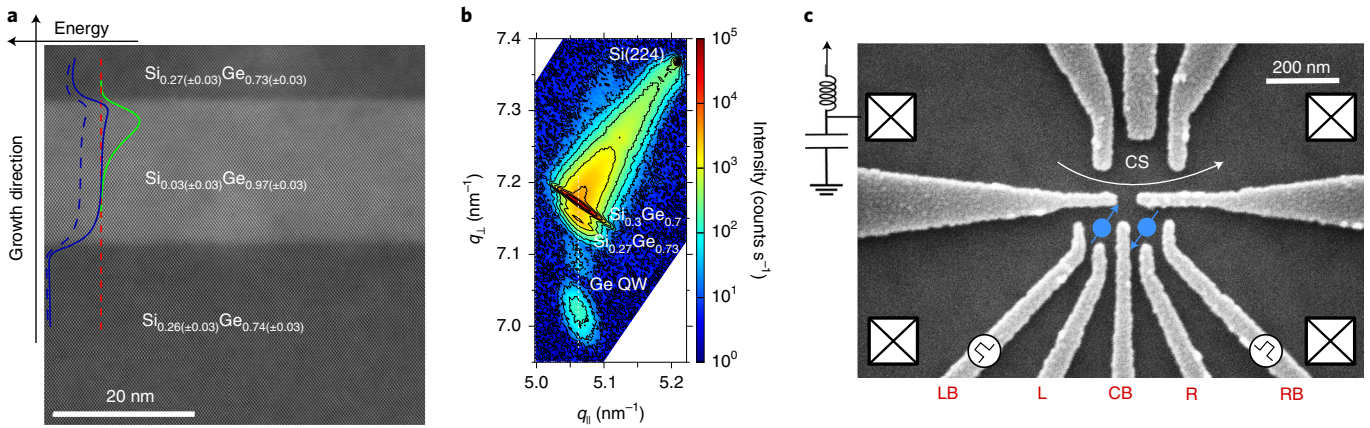
Fig. 1 | Heterostructure and gate layout. a, Atomic resolution HAADF scanning transmission electron microscopy image of the heterostructure showing sharp interfaces at the top and bottom of the QW. The stoichiometry of the three layers has been determined by electron energy-loss spectroscopy (Supplementary Fig. 5). The HH (solid blue line) and LH (dashed blue line) band energies as a function of growth direction are superimposed on the picture. The red dashed line represents the Fermi energy. HHs are accumulated at the upper QW interface, as shown by the bright green line representing the HH wavefunction density (simulations were performed in NextNano). **b**, X-ray diffraction reciprocal space map around the Si(224) Bragg peak, present at the top right of the map. $q_\perp$ and $q_{||}$ are, respectively, the out-of-plane (along [001]) and in-plane (along [110]) components of the X-ray scattering vector. The graded buffer is visible as a diffuse intensity between the Si peak and the $Si_{0.3}Ge_{0.7}$ peak, while the $Si_{0.3}Ge_{0.7}$ peak itself corresponds to the 2 μm constant composition layer at the top of the buffer. The Ge QW peak is aligned vertically below the $Si_{0.3}Ge_{0.7}$ virtual substrate, as shown by the dotted line, indicating that it has the same in-plane lattice parameter, that is, that the Ge QW is lattice-matched to the virtual substrate. The intensity just below the virtual substrate peak indicates that the true Ge content in the barriers on either side of the Ge QW is about 73%. The strain in the virtual substrate is zero; in the barrier, the in-plane strain is –0.15%; and in the Ge QW, it is –1.18%. **c**, Scanning electron microscope image of the gate layout used for this experiment. Voltages applied to gates LB, L, CB, R and RB form the double quantum dot potential where the hole spins (in blue) are confined. The rf-reflectometry circuit connected to the charge sensor (CS) ohmic (top left corner) is used for fast read-out. We note that without the application of any negative accumulation voltage, we measure a charge carrier density of 9.7×10^{11} cm^{-2}. Secondary ion mass spectroscopy rules out boron doping as a source for this carrier density. We thus attribute the measured hole density to the fixed negative charges in the deposited oxide, which can act as an accumulation gate[41].

Discussion Section 1). We set $\epsilon = 0$ at the $(2,0) \leftrightarrow (1,1)$ crossing. Starting from $(2,0)$, increasing ϵ mixes $(2,0)$ and $(1,1)$ into two molecular singlets, the ground state $S_G := S$ and the excited state S_E, neglected in the following, which are split at resonance by the tunnel coupling $2\sqrt{2}t_C$. The triplet states are almost unaffected by changes in ϵ. We define the exchange energy J as the energy difference between $S = \frac{1}{\sqrt{2}}(|\uparrow\downarrow\rangle - |\downarrow\uparrow\rangle)$ and the unpolarized triplet $T_0 = \frac{1}{\sqrt{2}}(|\uparrow\downarrow\rangle + |\downarrow\uparrow\rangle)$. At large positive detuning, J drops due to the decrease of the wavefunction overlap of the two separated holes. Importantly, different g factors for the left (g_L) and the right (g_R) dot result in four $(1,1)$ states: two polarized triplets, $|T_-\rangle = |\downarrow\downarrow\rangle$ and $|T_+\rangle = |\uparrow\uparrow\rangle$, and two anti-parallel spin states, $|\uparrow\downarrow\rangle$ and $|\downarrow\uparrow\rangle$ split by the Zeeman energy difference $\Delta E_Z = \Delta g \mu_B B$, where $\Delta g = |g_L - g_R|$, μ_B is the Bohr magneton and B is the magnetic field applied in the out-of-plane direction. However, as noticed later, even at large positive ϵ, a residual J persists, which leads to the total energy splitting between $|\uparrow\downarrow\rangle$ and $|\downarrow\uparrow\rangle$ being $E_{tot} = \sqrt{J(\epsilon)^2 + (\Delta g \mu_B B)^2}$.

By applying a pulse with varying ϵ (Fig. 2d) and stepping the magnetic field, we obtain the plot in Fig. 2e drawing a funnel. The experiment maps out the degeneracy between $J(\epsilon)$ and $E_Z^T = \pm \frac{\Sigma g \mu_B B}{2}$, where E_Z^T is the Zeeman energy of the polarized triplets and $\Sigma g = g_L + g_R$. The doubling of the degeneracy point can be attributed to fast spin–orbit induced $S - T_-$ oscillations[13]. At larger detuning, $S - T_0$ oscillations become visible.

The effective Hamiltonian of the qubit subsystem is

$$H = \begin{pmatrix} -J(\epsilon) & \frac{\Delta g \mu_B B}{2} \\ \frac{\Delta g \mu_B B}{2} & 0 \end{pmatrix} \qquad (1)$$

in the $\{|S\rangle, |T_0\rangle\}$ basis, with $J(\epsilon)$ being the detuning-dependent exchange energy, common to all $S - T_0$ qubits. Implementations of $S - T_0$ qubits in GaAs typically harvest the local field gradient

induced by the nuclear Overhauser field to drive $S - T_0$ oscillations[12,14]. Due to the near absence of nuclear spins in Si, only slow oscillations could be achieved in natural Si/SiGe structures[15]. Hence, micromagnets have been successfully used to enhance and stabilize the magnetic field gradient[16,17]. In Si metal–oxide–semiconductor devices, $S - T_0$ oscillations can be driven by spin–orbit induced g-factor differences in the two dots[18,19], and values of 20 MHz T^{-1} have been reported. Here, similarly, we realize $S - T_0$ oscillations through g-factor differences. However, we expect a larger Δg since our holes are of mainly HH character[20,21]. Indeed, as shown below, g-factor differences exceeding 20 GHz T^{-1} can be obtained. Pulsing on ϵ influences J, and the ratio between J and $\Delta g \mu_B B$ determines the rotation axis tilted by an angle $\theta = \arctan\left(\frac{\Delta g \mu_B B}{J(\epsilon)}\right)$ from the Z axis. For large detuning, $\theta \to 90°$, corresponding to X rotations, while for small detuning, $\theta \to 0°$, enabling Z rotations.

A demonstration of coherent Δg-driven rotations at a centre barrier voltage $V_{CB} = 910$ mV is depicted in Fig. 3c with the pulse sequence shown in Fig. 3b. The system is first initialized in $(2,0)$ in a singlet, then pulsed quickly deep into $(1,1)$, where the holes are separated. Here the state evolves in a plane tilted by θ (Fig. 3a,d). After a separation time τ_S, the system is brought quickly to the measurement point in $(2,0)$ where the Pauli spin blockade enables the distinction of triplet and singlet. Varying τ_S produces sinusoidal oscillations with frequency $f = \frac{1}{h}\sqrt{J^2 + (\Delta g \mu_B B)^2}$ (Fig. 3e), where h is the Planck constant. We extract $\Delta g = 2.04 \pm 0.04$ and $J(\epsilon = 4.5 \text{ meV}) \approx 21$ MHz. We attribute the large Δg to the different quantum dot sizes, which directly affect the HH–LH splitting, thus determining the effective g factor[10]. In addition, the different quantum dot charge occupations can lead to further g-factor differences[20,22] We approach frequencies of 100 MHz at fields as low as 3 mT. We observe similar values of Δg in the range of 1.0 to 2.7 in two additional devices with similar gate geometries (Supplementary Fig. 13). Figure 3f shows the
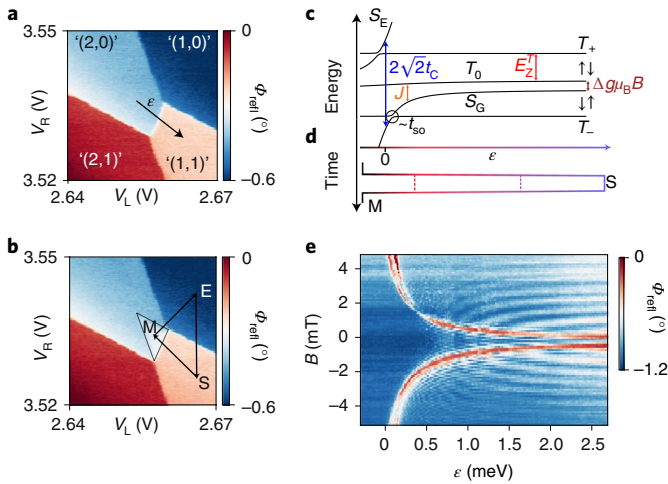
Fig. 2 | Pauli spin blockade and dispersion relation. a, Stability diagram of the region of interest. The effective number of holes in each Coulomb blocked island is defined as '(N_L,N_R)'. The quotes symbolize an equivalent hole number. The real hole number is $N_L = 3$ or 4 depending on the blockade region, and $N_R = 2n$ or $2n+1$ where n is an integer (also Supplementary Fig. 8). We will omit the quotes in the following. The diagonal arrow highlights the detuning (ϵ) axis. Pulses are added on gates LB and RB because of reduced cross-coupling to the opposite dot. The pulse amplitudes are calibrated with respect to the stability diagram acquired with L and R (Supplementary Fig. 7b). **b**, Stability diagram acquired while pulsing in a clockwise manner following the arrows. The system is emptied (E) in (1,0) and pulsed to (1,1) (separation point S), where either a singlet or a triplet will be loaded. Upon pulsing to the measurement point (M) in (2,0), the triplet states are blocked, leading to the marked triangular blockade region. **c**, Energy dispersion relation as a function of detuning ϵ at finite magnetic field. $\epsilon = 0$ is defined at the (2,0) ↔ (1,1) resonance. At high ϵ, the Hamiltonian has four eigenstates: two polarized triplets $|T_-\rangle = |\downarrow\downarrow\rangle$ and $|T_+\rangle = |\uparrow\uparrow\rangle$, and two anti-parallel spin states $|\uparrow\downarrow\rangle$ and $|\downarrow\uparrow\rangle$. The triplet Zeeman energy $E_Z^T = \pm \Sigma g \mu_B B/2$ (red) lifts the degeneracy of the triplets. The singlet energy $E_S = \frac{\epsilon}{2} - \sqrt{\frac{\epsilon^2}{4} + 2t_C^2}$, where t_C is the tunnel coupling between the dots, anti-crosses with the polarized triplet states (circled) due to a spin–orbit interaction parametrized by a spin-orbit spin flip tunnelling term t_{SO}. The singlet $S_G := S$ and triplet T_0 are split in energy by the exchange interaction $J = |E_S - E_{T_0}|$, which decreases with increasing ϵ. **d**, Pulse sequence adopted to acquire **e**. Starting from (2,0) the system is pulsed to (1,1) at varying ϵ (indicated by the dashed lines), left evolving for 100 ns and then pulsed back to measure in M. **e**, Spin funnel confirming **c** and the validity of assuming an effective hole number of (2,0) and (1,1). When $J(\epsilon) = E_Z^T$, the triplet signal (red) increases as a result of $S-T_-$ intermixing. Around the funnel, $S-T_-$ oscillations can be observed, while at higher detuning, $S-T_0$ oscillations become more prominent. In order to distinguish between $S-T_0$ and $S-T_-$ oscillations, we have applied detuning pulses with different ramp rates (Supplementary Fig. 14).

extracted singlet probability P_S at different magnetic fields. The black solid line is a fit to $P_S = A \cos(2\pi f \tau_S + \phi) \exp(-(t/T_2^*)^2) + C$, where T_2^* is the inhomogeneous dephasing time. P_S only oscillates between 0.5 and 1 as a direct consequence of $J(\epsilon = 4.5 \text{ meV}) \neq 0$ and the tilted rotation axis. One would expect an increase in the oscillation amplitude with higher magnetic field. However, at large ΔE_Z, the T_0 state quickly decays to the singlet during read-out due to relaxation processes[23], reducing the visibility, as is clearly shown by the curve at 2 mT in Fig. 3f. This can be circumvented by different read-out schemes such as latching[24] or shelving[25], but

this is out of the scope of the present work, which focuses on the low-magnetic-field behaviour.

We, furthermore, observe a dependence of Δg on the voltage on the centre barrier (CB) (Fig. 3g), confirming electrical control over the g factors. As the voltage is decreased by 50 mV, Δg varies from ~1.5 to more than 2.2, which conversely increases the frequency of X rotations. Concurrently we measure a similar trend in T_2^* reported at $B = 1$ mT in Fig. 3h; as the centre barrier is lowered, the coherence of the qubit is enhanced. The origin and consequences of this observation are discussed later.

Next, we demonstrate full access to the Bloch sphere, achieved by Z rotations leveraging the exchange interaction. We change the pulse sequence (Fig. 4b) such that after initialization in a singlet, the system is pulsed to large detuning, but is maintained in this position only for $t = t_{\pi/2}$ corresponding to a $\pi/2$ rotation, bringing the system close to $i|\uparrow\downarrow\rangle$. Now we let the state evolve for a time τ_S at a smaller detuning, increasing J and changing the rotation angle θ (Fig. 4d), before applying another $\pi/2$ rotation at high detuning and pulsing back to read-out. The state evolution on the Bloch sphere in Fig. 4a shows that full access to the qubit space can be obtained by a combination of appropriately timed pulses.

The resulting oscillation pattern is depicted in Fig. 4c. From the inferred frequency, we find the dependence of J on ϵ and extract $t_C/h = 3.64$ GHz as a free fitting parameter. The extracted values of J are plotted in Fig. 4e with the blue markers obtained from the exchange oscillation frequency. The green dots, on the other hand, correspond to $J(\epsilon) = E_Z^T = \frac{\Sigma g \mu_B B}{2}$ extracted from the funnel experiment (Fig. 2e). We find that the two sets of data points coincide when $\Sigma g = 11.0$. Together with the g-factor difference already reported, we obtain the two out-of-plane g factors to be 4.5 and 6.5, comparable to previous studies[21]. In Fig. 4f,g we plot P_S as a function of separation time at different values of ϵ. P_S now oscillates between 0 and 1 due to the combination of $\pi/2$ pulses and free evolution time at lower detuning. From the fits (black solid lines) at different detunings, we extract T_2^* as a function of ϵ (Fig. 4i). For low ϵ the coherence time is shorter than 10 ns, while it increases for larger ϵ and saturates at around 2 meV. This is explained by a simple noise model[14,16], where T_2^* depends on electric noise affecting J and a combination of electric and magnetic noise affecting ΔE_Z:

$$\frac{1}{T_2^*} = \frac{\pi\sqrt{2}}{h} \sqrt{\left(\frac{J(\epsilon)}{E_{\text{tot}}} \frac{dJ}{d\epsilon} \delta\epsilon_{\text{rms}}\right)^2 + \left(\frac{\Delta E_Z}{E_{\text{tot}}} \delta\Delta E_{Z\text{rms}}\right)^2}, \quad (2)$$

where $\delta\epsilon_{\text{rms}}$ is the root mean square (r.m.s.) noise on detuning, and $\delta\Delta E_{Z\text{rms}}$ describes the combination of electric noise on Δg and magnetic noise affecting B. We assume $\frac{d\Delta E_Z}{d\epsilon} \approx 0$ as we observe almost no change in Δg with detuning (Supplementary Fig. 9). From the fit (dark red solid line), we find $\delta\epsilon_{\text{rms}} = 7.59 \pm 0.35$ µeV, in line with comparable experiments[14,16], and $\delta\Delta E_{Z\text{rms}} = 1.78 \pm 0.10$ neV. Although $\delta\Delta E_{Z\text{rms}}$ is much smaller than $\delta\epsilon_{\text{rms}}$, we find that at large detuning, coherence is still limited by noise on ΔE_Z because $\frac{dJ}{d\epsilon} \to 0$ (red and violet dashed lines in Fig. 4i). We attribute the magnetic noise to randomly fluctuating hyperfine fields caused by spin-carrying isotopes in natural Ge, but a distinction from charge noise affecting Δg cannot be made here.

Equation (2) also gives insight into the trends observed in Fig. 3f,h. With B we now affect ΔE_Z and, thereby, its contribution to the total energy. The higher the ratio $\Delta E_Z/E_{\text{tot}}$, the more the coherence is limited by this term, as confirmed by the drop of T_2^* with magnetic field in Fig. 3f. Similarly one would expect that by increasing Δg, T_2^* should be lower. But, as shown in Fig. 4h, the increasing g-factor difference is accompanied by an increase of the tunnel coupling by 2 GHz. Hence, the increase of J is larger than the increase of ΔE_Z at lower V_{CB}, and $\frac{\Delta E_Z}{E_{\text{tot}}}$ is reduced, leading
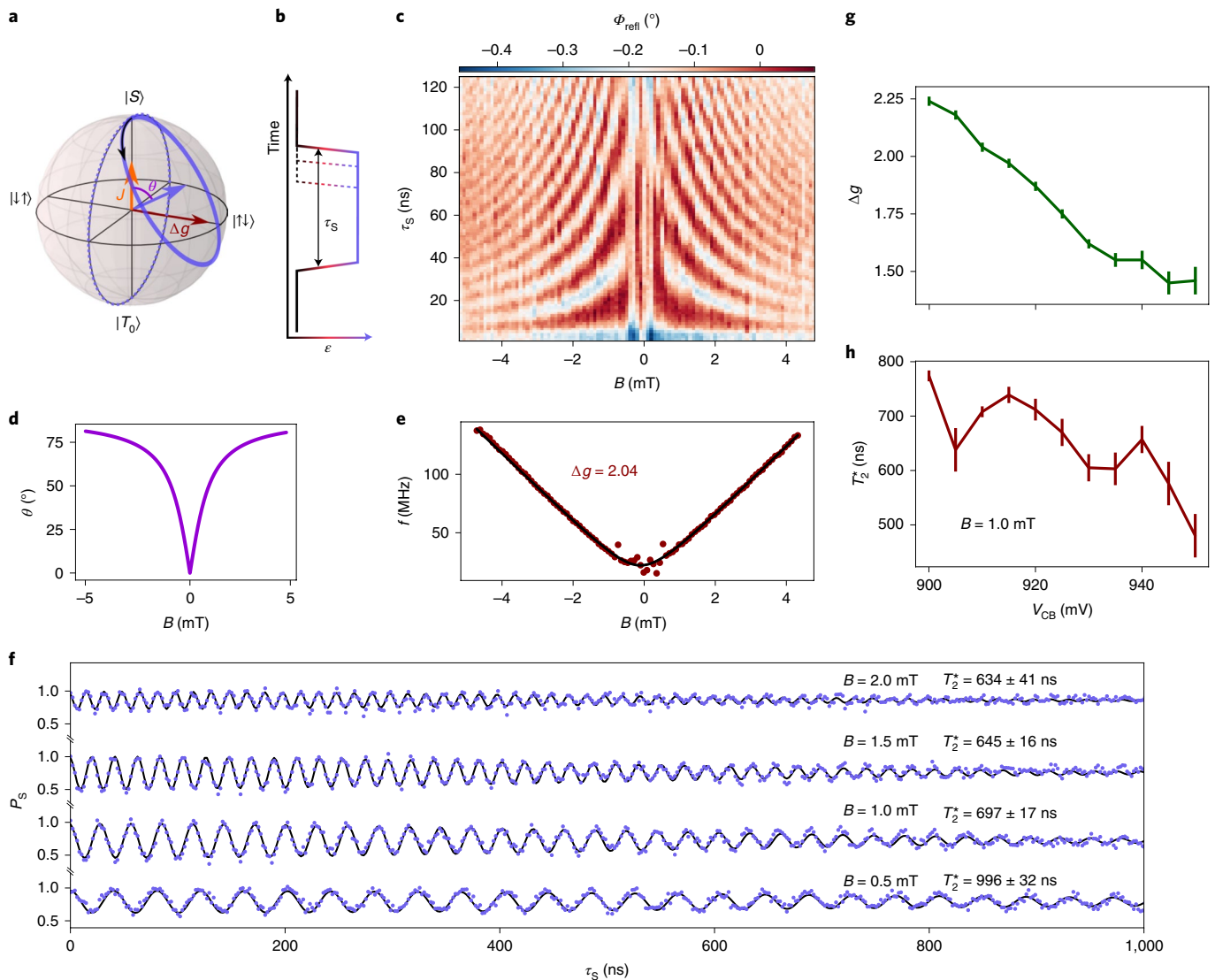
Fig. 3 | Δg-driven rotations. a, State evolution on the Bloch sphere. X rotations are controlled by Δg and the applied magnetic field. The ideal rotation axis is depicted as a dark red arrow. The dashed purple trajectory corresponds to a perfect X rotation while the effective rotation axis is tilted by an angle θ from the Z axis due to a finite residual J (orange arrow pointing along the Z axis) resulting in the state evolution depicted by the solid purple curve. **b**, Pulse sequence used for performing the Δg-driven rotations. The colour gradient is as in Fig. 2d. After initialization in a singlet, the separation time τ_S is varied (dashed lines) while the amplitude is $\epsilon = 4.5\,\text{meV}$. The system is then diabatically pulsed back to the measurement point. **c**, The Δg-driven oscillations as a function of magnetic field and separation time at $V_{CB} = 910\,\text{mV}$. The average of each column has been substracted to account for variations in the reflectometry signal caused by the magnetic field. A low (high) signal corresponds to a higher singlet (triplet) probability. Each point is integrated for 100 ms under continuous pulsing (Supplementary Fig. 17). **d**, $\theta = \arctan \frac{\Delta g \mu_B B}{J(2.8\,\text{meV})}$ versus magnetic field. The effective oscillation axis is magnetic-field dependent and approaches 80° for $B = 5\,\text{mT}$. **e**, Frequency of Δg-driven oscillations as a function of magnetic field (dark red dots). The black line is a fit to $f = \frac{1}{h}\sqrt{J^2 + (\Delta g \mu_B B)^2}$ where we extract a g-factor difference $\Delta g = 2.04 \pm 0.04$ and a residual exchange interaction $J(\epsilon = 4.5\,\text{meV}) = 20 \pm 1\,\text{MHz}$. We reach frequencies of 100 MHz at fields as low as 3 mT. **f**, Singlet probability P_S as a function of τ_S at different B fields for $V_{CB} = 910\,\text{mV}$ extracted through averaged single shot measurements (Supplementary Figs. 17 and 18). The solid lines are a fit to $P_S = A\cos(2\pi f \tau_S + \phi)\exp(-(t/T_2^*)^2) + C$, where A is the oscillation amplitude and C is an offset. Because of the tilted angle, P_S oscillates only between 0.5 and 1.0. Moreover, we observe a further decrease in visibility at higher magnetic fields due to decay mechanisms during the read-out process[23]. The extracted T_2^* shows a magnetic field dependence explainable by equation (2). **g**, The g-factor difference as a function of the centre barrier voltage V_{CB}. By opening the centre barrier, the g-factor difference increases from 1.50 to 2.25. Error bars correspond to one standard deviation. **h**, T_2^* versus V_{CB}. A near doubling in coherence time with lower centre barrier voltage is a consequence of an increased tunnel coupling (Fig. 4h) as explained in the main text. The error bars represent the confidence interval of the fits.

to a longer T_2^*. While V_{CB} affects both t_C and Δg, we see that V_{LB} and V_{RB}, where $V_{LB(RB)}$ is the voltage on gate LB (RB), affect mostly t_C and leave Δg unaltered (Supplementary Fig. 10). This exceptional tunability enables electrical engineering of the potential landscape to favour fast operations without negatively affecting the coherence times, thus enhancing the quality factor of this qubit. We find a quality factor $Q = f \times T_2^*$, that increases with magnetic field, reaching $Q = 52$ at 3 mT (Supplementary Fig. 15). While the longest T_2^* reported here is already comparable to electron singlet-triplet qubits in natural Si (ref. [17]), a reduction in the
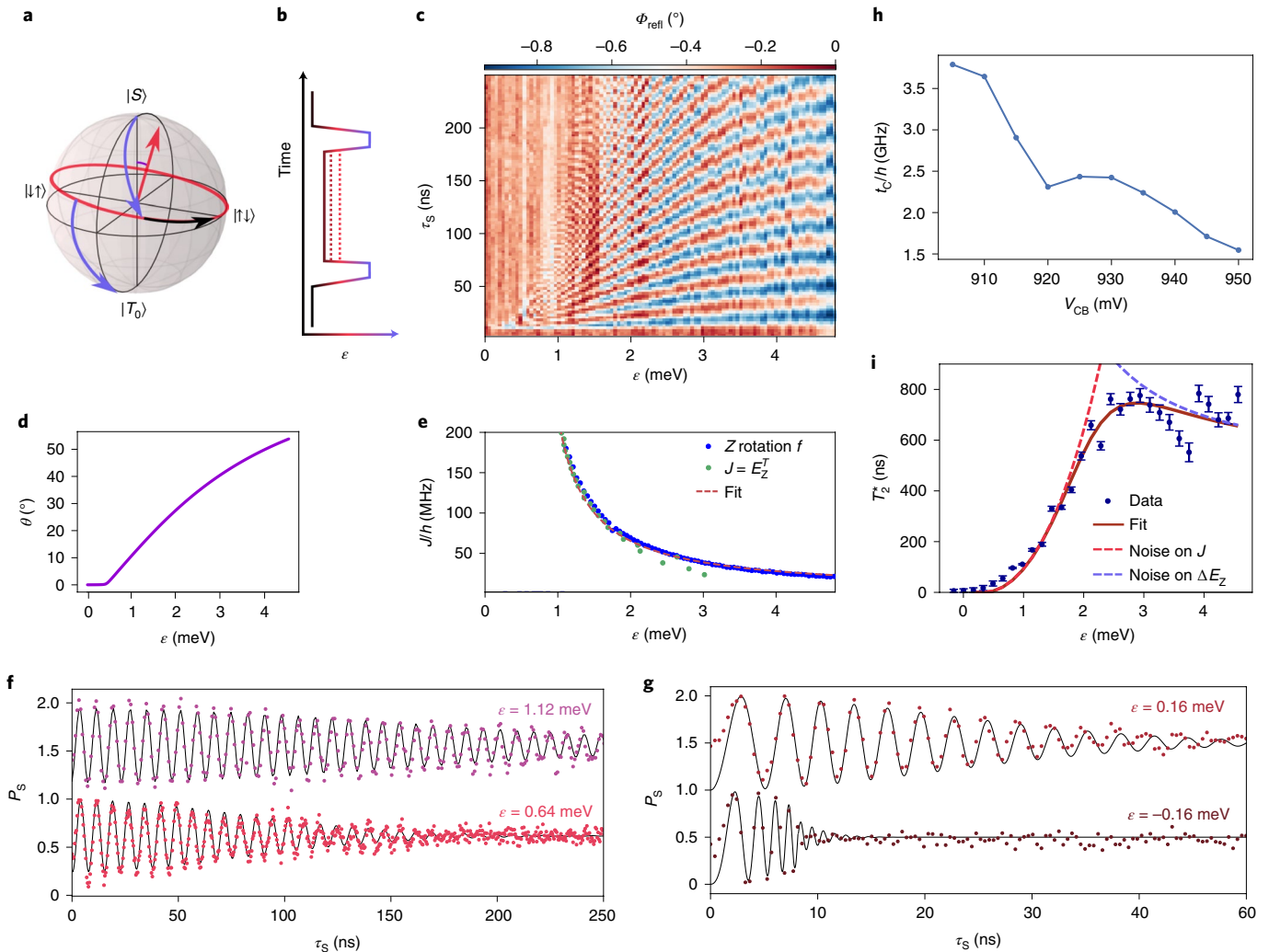
Fig. 4 | Exchange-rotations at $B = 1\,$mT and $V_{CB} = 910\,$mV. a, State evolution on the Bloch sphere. The purple arrows represent $\frac{\pi_x}{2}$ pulses applied at maximum detuning, while the red trajectory corresponds to the free evolution at smaller ϵ. The black arrow indicates the evolution of the state during the exchange pulse. **b**, Pulse sequence used to probe Z rotations. A $\frac{\pi_x}{2}$ pulse prepares the state close to the equator of the Bloch sphere, where it subsequently precesses under the influence of J at different ϵ as schematically indicated by the dashed lines. Another $\frac{\pi_x}{2}$ pulse maps the final state on the qubit basis for read-out. The colour gradient is as in Fig. 2d. **c**, Z rotations as a function of τ_S and ϵ. The acquisition method is the same as in Fig. 3c. **d**, Rotation angle θ as a function of ϵ for $B = 1\,$mT and J extracted from **c**. **e**, $J/h = \sqrt{f(\epsilon)^2 - (\Delta g \mu_B B/h)^2}$ as a function of ϵ as extracted from the oscillation frequency in **c** (blue markers). Green dots correspond to the spin funnel (Fig. 2e) condition $J(\epsilon) = E_Z^T$ with $\Sigma g = 11$, and the red dashed line is the best fit to $J(\epsilon) = \left| \frac{\epsilon}{2} - \sqrt{\frac{\epsilon^2}{4} + 2t_C^2} \right|$.

f,g, P_S as a function of τ_S for different ϵ. An offset of +1 was added to P_S for clarity. The pulse sequence adopted here increases the amplitude of oscillations as compared to Fig. 3f, enabling full access to the Bloch sphere. At very low ϵ, we observe the signal to chirp towards the correct frequency as a direct consequence of a finite pulse rise time. As a result, the coherence time is overestimated. **h**, Tunnel coupling t_C/h as a function of V_{CB}, demonstrating good control over the tunnel barrier between the two quantum dots. **i**, T_2^* as a function of ϵ. The dark red solid line is a fit to equation (2). We find $\delta\epsilon_{rms} = 7.59 \pm 0.49\,\mu$eV, in line with comparable experiments, and $\delta E_{Zrms} = 1.78 \pm 0.01\,$neV, smaller by a factor of two than in a comparable natural Si qubit[16]. The bright red (violet) dashed line represents the noise on J (ΔE_Z). For low detuning, clearly detuning charge noise on J dominates. At higher ϵ, the sum of electric noise acting on Δg and magnetic noise acting on B limit coherence. Error bars correspond to one standard deviation.

magnetic noise contribution by isotopic purification could further improve qubit dephasing and quality[18,19].

We now focus on extending the coherence of the qubit by applying refocusing pulses similar to those developed in nuclear magnetic resonance (NMR) experiments. We investigate the high ϵ region, where charge noise on detuning is lowest. Exchange pulses at $\epsilon = 0.64\,$meV are adopted as refocusing pulses. We note, however, that to obtain a perfect correcting pulse, it would be necessary to implement a more complex pulse scheme[26]. We choose convenient

τ_S values ($\tau_S = (2n + \frac{1}{2})t_{\pi_x}$, with n being an integer and t_{π_x} being the time needed for a π rotation along the x-axis) such that, if no decoherence has occurred, the system will always be found in the same state after τ_S. The refocusing pulse is then calibrated to apply a π pulse that brings the state on the same trajectory as before the refocusing pulse (Fig. 5a and Supplementary Fig. 16). The free evolution time after the last refocusing pulse τ_S' is varied in length from $\tau_S - \delta t$ to $\tau_S + \delta t$ (Fig. 5b,c), and we observe the amplitude of the resulting oscillations (Fig. 5e). Also, we increase the number of applied pulses
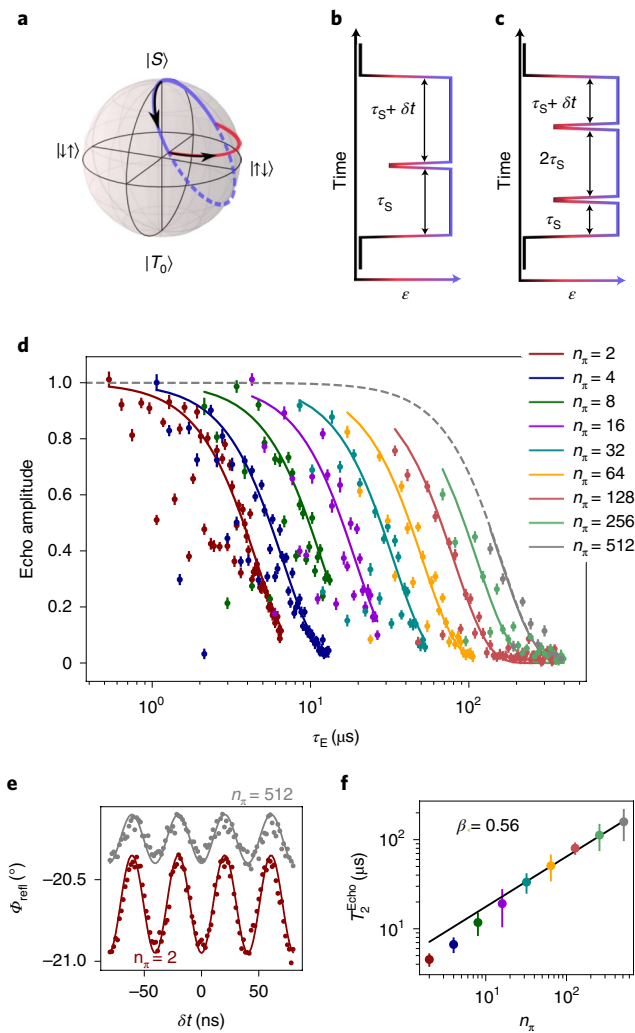
Fig. 5 | Spin echo at $B = 1$ mT. a, State evolution on the Bloch sphere. The state evolves on the violet trajectory. At appropriate times a short exchange pulse is applied, and the state follows the red trajectory instead of the dashed violet trajectory, followed by another free evolution on the violet trajectory. The free evolution times are chosen as $\tau_S = (2n + 1/2)t_{\pi_x}$, where t_{π_x} is the time needed for a π rotation along the violet trajectory. **b,c**, Pulse sequence for one and two refocusing pulses, respectively. The last free evolution is $\tau_S' = \tau_S + \delta t$. **d**, Normalized echo amplitude as a function of total separation time (τ_E) and colour-coded for number of refocusing pulses n_π. Solid lines are a fit to $A_E \exp\left(-t/T_2^{\mathrm{Echo}}\right)$ with A_E being the normalized echo amplitude. By increasing the number of π pulses from 2 to 512, the coherence time increases accordingly from $T_2^{\mathrm{Echo}}(n_\pi = 2) = 4.5 \pm 0.7$ µs (red) to $T_2^{\mathrm{Echo}}(n_\pi = 512) = 158.7 \pm 6.2$ µs (the grey solid line is the fit; the dashed grey line serves as guide to the eye). The error bars correspond to the confidence interval for the individual fits. **e**, Examples of $S - T_0$ oscillations as a function of δt taken for the first point of the red and grey datasets in **d**. For $n_\pi = 2$, $\Sigma\tau_S = 533$ ns, while for $n_\pi = 512$, $\Sigma\tau_S = 136$ µs. Solid lines are fit to the data, with the amplitude and phase as free parameters. **f**, Power law dependence of $T_2^{\mathrm{Echo}} = n_\pi^\beta$ with the same colour code as in **d**. The fitted β (black solid line) can be used to extract the noise spectral density dominated by low frequency $1/f$ noise for $n_\pi > 32$ [27]. The error bars correspond to the confidence interval of the fits of **d**.

from $n_\pi = 2$ to $n_\pi = 512$, thereby increasing the total free evolution time of the qubit and performing a Carr–Purcell–Meiboom–Gill echo. The decay is fitted to a Gaussian decay, and we extract the

echo coherence time T_2^{Echo} of 4.5 µs for $n_\pi = 2$ and T_2^{Echo} of 158 µs for $n_\pi = 512$. Furthermore, we observe a power law dependence of T_2^{Echo} as a function of the number of refocusing pulses and find $T_2^{\mathrm{Echo}} \approx n_\pi^\beta$ with a constant $\beta = 0.56$, suggesting a limitation by low frequency $1/f$ noise[27]. We note that for $n_\pi < 32$, we extract $\beta = 0.72$, being a signature of quasi-static noise with spectral density $\sim 1/f^2$.

In conclusion we have shown coherent two-axis control of a hole singlet-triplet qubit in Ge with an inhomogeneous dephasing time of 1 µs at 0.5 mT. We have taken advantage of an intrinsic property of HH states in Ge, namely their large and electrically tunable out-of-plane g factors. We achieved electrically driven Δg rotations of 150 MHz at fields of only 5 mT. Compared to Δg-driven singlet-triplet qubits in isotopically purified Si metal–oxide–semiconductor structures[18,19], we find a g-factor difference that is three orders of magnitude larger. Moreover, we demonstrate an electrical tunability of the g-factor difference ranging from 50% to more than 200% over a gate range of 50 mV in different devices. The large g-factor differences were confirmed in two additional devices underlining the reproducibility of the Ge platform. While varying g factors might be an obstacle to scale-up, the fast developing field of automated tuning[28] will be an asset in future experimental designs where g factors can be tailored in situ to the specific requirements. Echo sequences revealed a noise spectral density dominated largely by low frequency $1/f$ noise. The results and progress of singlet-triplet qubits, especially in the GaAs platform, will largely be applicable in Ge as well. Real-time Hamiltonian estimation[29] can boost T_2^*; a deeper understanding of the noise mechanisms might result in prolonging coherence even further[30]; and feedback-controlled gate operation could push gate fidelity beyond the threshold for fault tolerant computation[31].

In the future, a latched or shelved read-out could circumvent the decay of T_0 to the singlet during read-out, opening the exploration of the qubit's behaviour at slightly higher magnetic fields where the Δg rotation frequencies could surpass the highest electron-dipole spin-resonance Rabi frequencies reported so far[3,4], without suffering from reduced dephasing times. Furthermore, by moving towards symmetric operation or resonant driving, the quality of exchange oscillations can be increased, since the qubit is operated at an optimal working point[17,32–34]. The operation of Ge qubits at very low fields can further improve their prospects in terms of scalability and high-fidelity fast read-out, as it will facilitate their integration with superconducting circuits such as Josephson parametric amplifiers, superconducting resonators and superconducting quantum interference devices[35–40]. The long coherence times combined with fast and simple operations at extremely low magnetic fields make this qubit an optimal candidate for integration into a large-scale quantum processor.

Online content

Any methods, additional references, Nature Research reporting summaries, source data, extended data, supplementary information, acknowledgements, peer review information; details of author contributions and competing interests; and statements of data and code availability are available at https://doi.org/10.1038/s41563-021-01022-2.

References

1. Scappucci, G. et al. The germanium quantum information route. *Nat. Rev. Mater.* https://doi.org/10.1038/s41578-020-00262-z (2020).
2. Kloeffel, C., Trif, M. & Loss, D. Strong spin-orbit interaction and helical hole states in Ge/Si nanowires. *Phys. Rev. B* **84**, 195314 (2011).
3. Froning, F. N. M. et al. Ultrafast hole spin qubit with gate-tunable spin–orbit switch functionality. *Nat. Nanotechnol.* **16**, 308–312 (2021).
4. Wang, Z. et al. Optimal operation points for ultrafast, highly coherent Ge hole spin-orbit qubits. *npj Quantum Inf.* **7**, 54 (2021).

5. Lodari, M. et al. Light effective hole mass in undoped Ge/SiGe quantum wells. *Phys. Rev. B* **100**, 041304(R) (2019).
6. Loss, D. & DiVincenzo, D. P. Quantum computation with quantum dots. *Phys. Rev. A* **57**, 120–126 (1998).
7. Hendrickx, N. W. et al. A four-qubit germanium quantum processor. *Nature* **591**, 580–585 (2021).
8. Watzinger, H. et al. A germanium hole spin qubit. *Nat. Commun.* **9**, 3902 (2018).
9. Hendrickx, N. W., Franke, D. P., Sammak, A., Scappucci, G. & Veldhorst, M. Fast two-qubit logic with holes in germanium. *Nature* **577**, 487–491 (2020).
10. Katsaros, G. et al. Observation of spin-selective tunneling in SiGe nanocrystals. *Phys. Rev. Lett.* **107**, 246601 (2011).
11. Levy, J. Universal quantum computation with spin-1/2 pairs and Heisenberg exchange. *Phys. Rev. Lett.* **89**, 147902 (2002).
12. Petta, J. R. Coherent manipulation of coupled electron spins in semiconductor quantum dots. *Science* **309**, 2180–2184 (2005).
13. Petta, J. R., Lu, H. & Gossard, A. C. A coherent beam splitter for electronic spin states. *Science* **327**, 669–672 (2010).
14. Dial, O. E. et al. Charge noise spectroscopy using coherent exchange oscillations in a singlet-triplet qubit. *Phys. Rev. Lett.* **110**, 146804 (2013).
15. Maune, B. M. et al. Coherent singlet-triplet oscillations in a silicon-based double quantum dot. *Nature* **481**, 344–347 (2012).
16. Wu, X. et al. Two-axis control of a singlet-triplet qubit with an integrated micromagnet. *Proc. Natl Acad. Sci. USA* **111**, 11938–11942 (2014).
17. Takeda, K., Noiri, A., Yoneda, J., Nakajima, T. & Tarucha, S. Resonantly driven singlet-triplet spin qubit in silicon. *Phys. Rev. Lett.* **124**, 117701 (2020).
18. Jock, R. M. et al. A silicon metal-oxide-semiconductor electron spin-orbit qubit. *Nat. Commun.* **9**, 1768 (2018).
19. Harvey-Collard, P. et al. Spin-orbit interactions for singlet-triplet qubits in silicon. *Phys. Rev. Lett.* **122**, 217702 (2019).
20. Watzinger, H. et al. Heavy-hole states in germanium hut wires. *Nano Lett.* **16**, 6879–6885 (2016).
21. Hofmann, A. et al. Assessing the potential of Ge/SiGe quantum dots as hosts for singlet-triplet qubits. Preprint at https://arxiv.org/abs/1910.05841 (2019).
22. Liles, S. D. et al. Spin and orbital structure of the first six holes in a silicon metal-oxide-semiconductor quantum dot. *Nat. Commun.* **9**, 3255 (2018).
23. Barthel, C. et al. Relaxation and readout visibility of a singlet-triplet qubit in an Overhauser field gradient. *Phys. Rev. B* **85**, 035306 (2012).
24. Studenikin, S. A. et al. Enhanced charge detection of spin qubit readout via an intermediate state. *Appl. Phys. Lett.* **101**, 233101 (2012).
25. Orona, L. A. et al. Readout of singlet-triplet qubits at large magnetic field gradients. *Phys. Rev. B* **98**, 125404 (2018).
26. Wang, X. et al. Composite pulses for robust universal control of singlet–triplet qubits. *Nat. Commun.* **3**, 997 (2012).
27. Yoneda, J. et al. A quantum-dot spin qubit with coherence limited by charge noise and fidelity higher than 99.9%. *Nat. Nanotechnol.* **13**, 102–106 (2017).
28. Moon, H. et al. Machine learning enables completely automatic tuning of a quantum device faster than human experts. *Nat. Commun.* **11**, 4161 (2020).
29. Shulman, M. D. et al. Suppressing qubit dephasing using real-time Hamiltonian estimation. *Nat. Commun.* **5**, 5156 (2014).
30. Bluhm, H. et al. Dephasing time of GaAs electron-spin qubits coupled to a nuclear bath exceeding 200 μs. *Nat. Phys.* **7**, 109–113 (2010).
31. Cerfontaine, P. et al. Closed-loop control of a GaAs-based singlet-triplet spin qubit with 99.5% gate fidelity and low leakage. *Nat. Commun.* **11**, 4144 (2020).
32. Martins, F. et al. Noise suppression using symmetric exchange gates in spin qubits. *Phys. Revi. Lett.* **116**, 116801 (2016).
33. Reed, M. et al. Reduced sensitivity to charge noise in semiconductor spin qubits via symmetric operation. *Phys. Rev. Lett.* **116**, 110402 (2016).
34. Nichol, J. M. et al. High-fidelity entangling gate for double-quantum-dot spin qubits. *npj Quantum Inf.* **3** 3 (2017).
35. Wallraff, A. et al. Strong coupling of a single photon to a superconducting qubit using circuit quantum electrodynamics. *Nature* **431**, 162–167 (2004).
36. Stehlik, J. et al. Fast charge sensing of a cavity-coupled double quantum dot using a Josephson parametric amplifier. *Phys. Rev. Appl.* **4**, 014018 (2015).
37. Burkard, G., Gullans, M. J., Mi, X. & Petta, J. R. Superconductor–semiconductor hybrid-circuit quantum electrodynamics. *Nat. Rev. Phys.* **2**, 129–140 (2020).
38. Leonard, E. et al. Digital coherent control of a superconducting qubit. *Phys. Rev. Appl.* **11**, 014009 (2019).
39. Schupp, F. J. et al. Sensitive radiofrequency readout of quantum dots using an ultra-low-noise SQUID amplifier. *J. Appl. Phys.* **127**, 244503 (2020).
40. Vigneau, F. et al. Germanium quantum-well Josephson field-effect transistors and interferometers. *Nano Lett.* **19**, 1023–1027 (2019).
41. Amitonov, S. V., Spruijtenburg, P. C., Vervoort, M. W. S., van der Wiel, W. G. & Zwanenburg, F. A. Depletion-mode quantum dots in intrinsic silicon. *Appl. Phys. Lett.* **112**, 023102 (2018).

Methods

QW growth. In contrast with the Ge QWs previously employed for qubit fabrication[1], in the present study, the strained Ge QW structure was grown by low-energy plasma-enhanced chemical vapour deposition[42] instead of thermal chemical vapour deposition. The buffer between the Si(001) wafer and the Ge QW structure is a graded region approximately 10 μm thick in which the Ge content was increased linearly from pure Si up to the desired final composition of $Si_{0.3}Ge_{0.7}$. Buffers grown with thermal chemical vapour deposition typically exploit a reverse-graded approach starting from a thick pure-Ge layer on the Si(001) wafer[43]. As a consequence, the Ge content in the SiGe spacers used here is approximately 70%, a lower value than the 80% used in previous reports. This will induce larger strain in the Ge QW[44] and therefore a larger energy difference between HH and LH states, an important feature in order to engineer as pure as possible HH states with large out-of-plane g factors and g-factor differences. In the case of Ge QWs grown by thermal chemical vapour deposition on reverse-graded buffers, the buffer and SiGe spacers tend to display a small residual tensile strain[45].

The substrate temperature was reduced from 760 to 550 °C with increasing Ge content. The buffer was completed with a 2 μm region at a constant composition of $Si_{0.3}Ge_{0.7}$. This part was concluded in about 30 min, with a growth rate of $5–10\,nm\,s^{-1}$ due to the efficient dissociation of the precursor gas molecules by the high-density plasma. The graded virtual substrate typically presents a threading dislocation density of about $5\times10^6\,cm^{-2}$ (ref. [46]). The substrate temperature and plasma density was then reduced without interrupting the growth. The undoped $Si_{0.3}Ge_{0.7}/Ge/Si_{0.3}Ge_{0.7}$ QW stack was grown at 350 °C and a growth rate of about $0.5\,nm^{-1}$ to limit Si intermixing and interface diffusion. A 2 nm Si cap was deposited after a short (60 s) interruption to facilitate the formation of the native oxide (the interruption reduces Ge contamination in the Si cap from residual precursor gases in the growth chamber). Secondary ion mass spectroscopy analysis indicates that boron levels are below the detection limit of $10^{15}\,cm^{-3}$ to a depth of at least 200 nm.

Device fabrication. The samples were processed in the Institute of Science and Technology Austria Nanofabrication Facility. A $6\times6\,mm^2$ chip is cut out from a four inch wafer and cleaned before further processing. The ohmic contacts are first patterned in a 100 keV electron beam lithography system; then a few nanometres of native oxide and the SiGe spacer is milled down by argon bombardment, and subsequently a layer of 60 nm Pt is deposited in situ at an angle of 5°, to obtain reproducible contacts. No additional intentional annealing is performed. A mesa of 90 nm is etched in a reactive ion etching step. The native SiO_2 is removed by a 10 s dip in buffered HF before the gate oxide is deposited. The oxide is a 20 nm atomic-layer-deposited aluminium oxide (Al_2O_3) grown at 300 °C, which unintentionally anneals the ohmic contacts, resulting in a low-resistance contact to the carriers in the QW. The top gates are first patterned via electron beam lithography and then a Ti/Pd 3/27 nm layer is deposited in an electron beam evaporator. The thinnest gates are 30 nm wide and 30 nm apart. An additional thick gate metal layer is subsequently written and deposited and serves to overcome the mesa step and allow wire bonding of the sample without shorting the gates together. Quantum dots are formed by means of depletion gates (Fig. 1c). The lower gates (LB, L, CB, R, RB) form a double quantum dot system, and the upper gates tune a charge sensor (CS) dot. The separation gates in the middle are tuned to maximize the CS sensitivity to charge transitions in the double quantum dot. An inductance-capacitance (*LC*) circuit connected to a CS ohmic contact allows fast read-out through microwave reflectometry. LB and RB are further connected to fast gate lines, enabling fast control of the energy levels in the double quantum dot.

Data availability

All data included in this work are available from the Institute of Science and Technology Austria repository[47].

References

42. Rössner, B., Chrastina, D., Isella, G. & von Känel, H. Scattering mechanisms in high-mobility strained Ge channels. *Appl. Phys. Lett.* **84**, 3058–3060 (2004).
43. Shah, V. A. et al. Reverse graded relaxed buffers for high Ge content SiGe virtual substrates. *Appl. Phys. Lett.* **93**, 192103 (2008).
44. Wang, Z. et al. Optimal operation points for ultrafast, highly coherent Ge hole spin-orbit qubits. Preprint at https://arXiv:1911.11143 (2019).
45. Sammak, A. et al. Shallow and undoped germanium quantum wells: a playground for spin and hybrid quantum technology. *Adv. Funct. Mater.* **29**, 1807613 (2019).
46. Marchionna, S., Virtuani, A., Acciarri, M., Isella, G. & von Kaenel, H. Defect imaging of SiGe strain relaxed buffers grown by LEPECVD. *Mater. Sci. Semicond. Process.* **9**, 802–805 (2006).
47. Jirovec, D. Research data for "A singlet-triplet hole spin qubit planar Ge". https://doi.org/10.15479/AT:ISTA:9323 (2021).

Acknowledgements

Author contributions

D.J. fabricated the sample and performed the experiments and data analysis. D.J., A.H. and I.P. developed the fabrication recipe. D.J., A.H., O.S. and M. Borovkov performed precharacterizing measurements on equivalent samples. J.S.-M. and G.K. fabricated the two additional devices discussed in the Supplementary Information. J.K. performed the experiments on those additional devices. D.C. and A.B. designed the SiGe heterostructure. A.B. performed the growth, supervised by G.I.; D.C. performed the X-ray diffraction measurements and simulations. G.T. performed Hall effect measurements, supervised by D.C.; P.M.M. derived the theoretical model. M. Botifoll and J.A. performed the atomic resolution scanning transmission electron microscopy structural and electron energy-loss spectroscopy compositional related characterization and calculated the strain by using geometrical phase analysis. D.J., A.H., J.K., A.C., F.M., J.S.-M. and G.K. discussed the qubit data. D.J. and G.K. wrote the manuscript with input from all the authors. G.I. and G.K. initiated and supervised the project.

Competing interests

The authors declare no competing interests.

Additional information